

On the Dependence of Squall-Line Characteristics on Surface Conditions

KARSTEN PETERS AND CATHY HOHENEGGER

Max-Planck-Institut für Meteorologie, Hamburg, Germany

(Manuscript received 13 October 2016, in final form 13 April 2017)

ABSTRACT

The influence of surface conditions in the form of changing surface temperatures on fully developed mesoscale convective systems (MCSs) is investigated using a cloud-system-resolving setup of the Icosahedral Nonhydrostatic (ICON) model (1-km grid spacing). The simulated MCSs take the form of squall lines with trailing stratiform precipitation. After the squall lines have reached a quasi-steady state, secondary convection is triggered ahead of the squall line, resulting in an increase of squall-line propagation speed, also known as discrete propagation. The higher propagation speed is then maintained for the remainder of the simulations because secondary convection ahead of the squall line acts to reduce the environmental wind shear over the depth of the squall line's cold pool. The surface conditions have only a marginal effect on the squall lines themselves. This is so because the surface fluxes cannot significantly affect the cold pool, which is continuously replenished by midtropospheric air. The midtroposphere remains similar given the use of identical initial profiles. The only effect of the surface fluxes consists in an earlier acceleration of the squall line due to earlier initiation of secondary convection with higher surface temperature. Finally, a conceptual model to estimate the change in surface temperature needed to achieve a change in onset time of prefrontal secondary convection and the associated discrete propagation events given the environmental conditions is presented.

1. Introduction

The interaction between the atmosphere and the underlying land surface is determined by energy exchanges via sensible and latent heat fluxes, the exertion of drag forces due to surface roughness and the coupling of these processes to planetary boundary layer (PBL) dynamics and atmospheric convection. In numerical atmospheric models—for example, those used for numerical weather prediction (NWP)—these interactions are subgrid processes because their spatial scales are typically smaller than those offered by the model grid spacing. Thus, the representation of land–atmosphere interactions in such models depends on the interplay of a suite of parameterization schemes that introduces uncertainties into the model solution by design (e.g., [Betts and Jakob 2002](#); [Hohenegger et al. 2009](#); [Pearson et al. 2014](#)). Reducing these uncertainties resulting from deficiencies in parameterization design and coupling is therefore of utmost importance to increase confidence in weather forecasts and climate projections ([Jakob 2010, 2014](#)).

Surface fluxes modify PBL characteristics and thereby exert strong controls on the preconditioning of the atmosphere toward the triggering of deep convection (e.g., [Tawfik and Dirmeyer 2014](#)). As a result, uncertainties inherent in boundary layer parameterization schemes become especially apparent when investigating atmospheric convection. On one end of the spectrum of convective processes in models, these uncertainties occur at the model grid scale and impact the representation of individual convective elements. On the other end of the spectrum, MCSs such as squall lines cover spatial scales far beyond those resolved by the model grid spacing, propagate fairly rapidly, and, therefore, encounter a variety of different land surface conditions. An adequate representation of land–atmosphere coupling is therefore essential for NWP.

With this study we contribute to the reduction of uncertainties in the representation of convective processes in large-scale atmospheric models by investigating the influence of surface temperatures on mature squall lines. We perform idealized simulations with the Icosahedral Nonhydrostatic (ICON) modeling system ([Zängl et al. 2015](#)) at cloud-system-resolving resolution (1 km). In this modeling framework, only surface processes are parameterized—the employed horizontal and vertical

Corresponding author: Karsten Peters, karsten.peters@mpimet.mpg.de

grid spacings do not require PBL dynamics and atmospheric convection to be parameterized.

A systematic and thorough evaluation of the influence of surface properties on squall lines employing idealized frameworks is absent in the literature. Surface flux influences on squall lines simulated in idealized model setups have been neglected in past studies so as to focus on other influences, like environmental conditions, model grid spacing, and the parameterization of turbulence or of microphysics (e.g., Rotunno et al. 1988; Weisman et al. 1997; Weisman and Rotunno 2004; Takemi 2007; Bryan and Morrison 2012; Verrelle et al. 2015; Alfaro and Khairoutdinov 2015; Alfaro 2017).

This does not mean that the impact of the land surface on squall lines and MCSs in general has not been studied. In fact, this has been done for a selected number of case studies inspired by observations. Trier et al. (1996) performed simulations of a squall line observed during the TOGA COARE field campaign (Webster and Lukas 1992) and investigated the influence of surface fluxes and stresses generated by the squall line itself on the model solution—most notably, including the surface fluxes-induced changes in the extent and structure of the squall-line-generated cold pool. Approximating environmental conditions typical for the Sahel region, Clark et al. (2004) determined the influence of altered surface properties on the PBL structure and then exposed a fully developed squall line to the changed PBL. They concluded that in order for the changes in PBL structure to influence the squall line, the spatial scales of the perturbations should be on the order of the convection itself, that is, $O(10)$ km. On the contrary, Wolters et al. (2010) showed that differences in large-scale soil moisture gradients $O(100)$ km can have profound influences on the propagation of and precipitation associated with West African squall lines. Lauwaet et al. (2010) and Adler et al. (2011) analyzed a particular case of an MCS in western Africa, which occurred during the African Monsoon Multidisciplinary Analysis (AMMA; Redelsperger et al. 2006) field campaign. On the one hand, Lauwaet et al. (2010) used cloud-system-resolving simulations (3-km grid spacing; cumulus parameterization turned off) to investigate the impact of enhanced and reduced vegetation cover on the properties of an MCS. They found that for an increase in vegetation, MCS rainfall scales approximately with the increase in near-surface moistening. With the reduction of vegetation however, rainfall remained at the level of the control simulation because the drier PBL led to more intense convectively generated cold pools, which helped to maintain the strength of the MCS despite the reduced latent heat flux. Adler et al. (2011), on the other hand, investigated the impact of soil moisture distributions.

Among other experiments, they reduced or enhanced soil moisture in a band of 2° zonal width in the path of the MCS and found that this soil moisture inhomogeneity has remote influence on the rainfall of the approaching MCS. Rather than modifying surface properties directly, Oberthaler and Markowski (2013) investigated the influence of anvil shading on squall-line properties in simulations of a squall-line case observed over Oklahoma. In the prefrontal environment, anvil shading led to a reduction of surface temperatures, leading to reduced turbulent mixing near the surface that altered the near-surface wind shear. Such modifications to the wind shear profile over the depth of the cold pool can influence the propagation characteristics of a squall line [see Rotunno et al. (1988) and section 4 of the present study].

All of the above studies associate the influence of surface fluxes on squall lines with the modification of the PBL structure ahead of the convective system. However, another way surface fluxes could act to influence squall lines is by directly modifying one of its key features, namely, the convectively generated cold pool. The strength and stratification of the cold pool are understood as being important determinants of a squall line's intensity, propagation speed, and longevity (Rotunno et al. 1988; Fovell and Ogura 1989; Weisman and Rotunno 2004; Alfaro and Khairoutdinov 2015; Alfaro 2017). Modification of the cold pool by surface fluxes could thus affect squall-line properties (Trier et al. 1996). Recent modeling studies investigated the impact of surface fluxes on cold pools that were either generated by "popcorn" cumulus convection (Gentine et al. 2016; sensible and latent heat fluxes) or initiated by a cold bubble (Grant and van den Heever 2016; sensible heat flux only). As expected, surface fluxes act to reduce the strength of the simulated cold pools by either just heating (Grant and van den Heever 2016) or heating and moistening (Gentine et al. 2016) of the near-surface air. However, once these cold pools were established in the simulations, they were not continuously replenished by cold downdraft air stemming from the midtroposphere as is the case for squall lines [Houze (2014) and references therein]. As the strength of convectively generated cold pools is mainly determined by the thermodynamic properties of the air where the convective downdrafts originate (e.g., Takemi 2007; Schlemmer and Hohenegger 2014; Alfaro and Khairoutdinov 2015), it is not clear how strongly surface heating can counteract this constant supply of cold air to the cold pool.

From these previous studies, two pathways for surface fluxes to influence the morphology and kinematics of a squall line emerge:

- 1) modification of the PBL structure ahead of the squall line and
- 2) weakening of the convectively generated cold pool.

A thorough investigation of these points has not been performed yet. Here we address them by simulating squall lines in an idealized setting using the ICON model at cloud-system-resolving resolutions (section 2). We show in section 3 that our simulation setup allows us to simulate squall lines with trailing stratiform precipitation with the salient features as described in earlier studies, including the initiation of secondary convection ahead of the squall line and associated abrupt acceleration of the squall line called discrete propagation in past studies (Zipser 1977; Houze 1977; Carbone et al. 1990; Grady and Verlinde 1997; Fovell et al. 2006). We subject the squall lines to different surface temperatures and find that the only way the surface affects the squall-line characteristics is by altering the initiation time of secondary convection ahead of the squall lines (section 4). In short, stronger surface heating preconditions the atmosphere toward the triggering of deep convection, thereby setting the stage for the occurrence of convective initiation ahead of the squall line, which leads to discrete propagation events and an overall acceleration of the squall line due to modification of the environmental wind profile (section 5). From this, we propose a linear relationship that provides a link between the change in time of the occurrence of secondary convection ahead of the squall line and the change in surface temperature needed to achieve it (section 6). Such a metric could be used to aid the short term prediction of severe weather events. We conclude and discuss the results in section 7.

2. Methodology

We apply the ICON modeling system at a cloud-system-resolving resolution of 1 km in a similar version as in Dipankar et al. (2015). Given the results of Bryan et al. (2003), who performed large-eddy simulations of squall lines with grid spacings between 125 m and 1 km, the use of 1-km grid spacing is sufficient to reproduce the general characteristics of simulated squall lines. Parameterizations of atmospheric radiation, convection, and cloud cover are not employed in our simulations. Subgrid turbulence is calculated following the classical Smagorinsky approach and cloud microphysics treat cloud and rainwater as well as cloud ice and snow in a single-moment scheme (Doms et al. 2011). We perform all simulations in a strongly idealized setting in which we neglect radiative processes for simplicity and apply a fixed surface temperature T_S with surface fluxes being

computed following the drag-law formulation [cf. Dipankar et al. (2015), their Eqs. (33) and (34)]; that is, the interaction between the surface and the atmosphere is one way as opposed to two way if an interactive land surface were used. The roughness length is set to $z_0 = 10^{-3}$ m. The latent heat flux is computed assuming saturation with respect to water vapor at the surface. Motivated by the results of Gentine et al. (2016) and Grant and van den Heever (2016), who investigated the influence surface fluxes on cold pools, the lower-boundary condition we apply here maximizes the possible effects of surface fluxes on the cold pool associated with the squall line because sensible and latent heat fluxes are maximized [fixed T_S and saturation with respect to water vapor at the surface; compare with Del Genio et al. (2012) regarding the impact of water versus land surfaces on the recovery of convective cold pools]. In reality, the effects would be weaker. The simulation domain (x - y) measures 700×500 grid points. The triangular grid cells used in ICON have an edge length of 1 km, resulting in a domain size (x - y) of 700×433 km². We confirmed that our results do not depend on domain size by performing a simulation where we doubled the domain edge lengths. The model top is at 20 km and we use 100 vertical levels with variable spacing ranging from 20 to 561 m for the lowest and the highest model levels, respectively. We use a time step of 5 s and the model simulations are integrated for 9 h. We output instantaneous two- and three-dimensional fields every 10 min. We apply doubly periodic boundary conditions. In the forthcoming analysis, all distances are given with respect to the domain center at ($x = 0$ km, $y = 0$ km).

To initiate the development of a self-contained squall-line system, we apply the test case methodology of Weisman and Klemp (1982, hereafter WK82). The WK82 test case consists of a rising warm bubble in an environment characterized by an initial analytical sounding representative of unstable midlatitude conditions together with a wind profile featuring unidirectional shear in the x direction. We initiate the warm bubble as described in WK82—that is, an axially symmetric thermal perturbation of +2-K magnitude with 10-km horizontal and 1.4-km vertical radii. The center of the bubble lies at 1.4 km above sea level and is located at (−100, 0) km in the simulation domain. The initial sounding and wind profile are specified as in WK82 and shown in Fig. 1. In particular, the maximum water vapor mixing ratio is set to $q_{v,\max} = 14$ g kg^{−1} and the maximum of the wind profile is set to $U_{\max} = 10$ m s^{−1}. The original WK82 test case setup does not account for any surface interactions. This condition does not apply in our simulations (see above), where surface fluxes are

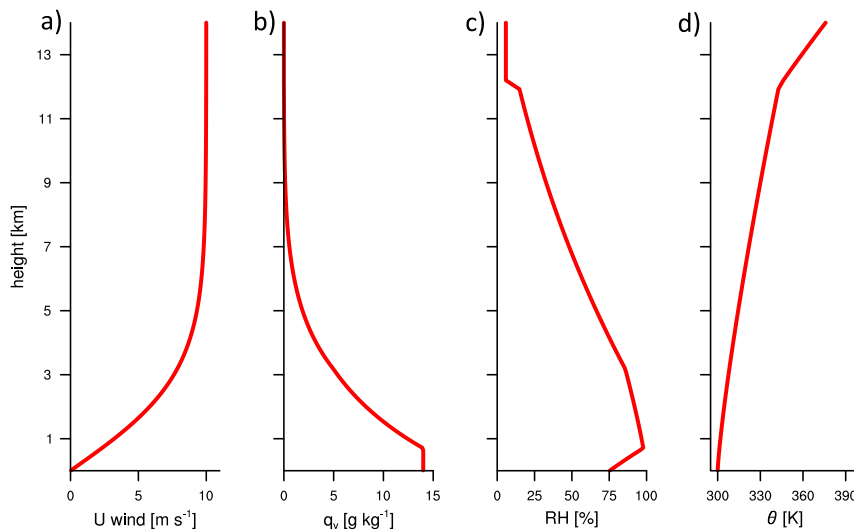


FIG. 1. Atmospheric profiles of (a) u wind (m s^{-1}), (b) specific humidity q_v (g kg^{-1}), (c) relative humidity (RH; %), and (d) potential temperature θ (K) used as initial conditions in the numerical experiments. The atmospheric profiles follow the analytic formulations given in WK82.

accounted for. In fact, including surface friction in our simulations induces turbulent mixing in the near-surface air layer, which acts to homogenize the lowermost wind profile and thereby to reduce the shear. This effect remains constrained to the lowest 1 km above the surface in the simulation.

The rising warm-air bubble leads to the initiation of a first convective storm, which weakens and then redevelops and again dissipates. The radially expanding convective outflow of this first convective storm leads to the development of convective features propagating away from the location of the initial warm bubble. The convection propagating parallel to the environmental wind direction in positive x direction interacts with the low-level wind shear and eventually organizes into a squall line (cf. section 3a).

The analysis focuses on the propagation of this squall line. All of the analysis presented here is performed in a subdomain—the “domain” in the following—measuring 315 km (from -120 to 195 km) in the x direction and 60 km (from -30 to 30 km) in the y direction. The domain fully contains the squall line and its propagation. We focus on this domain to ensure the analysis of a linear convective structure in y direction propagating perpendicular to the environmental wind field in positive x direction (cf. the spatial structure of convection shown in Fig. 4).

We perform simulations with $T_S = 299, 300, 301,$ and 301.5 K. The control simulation features $T_S = 300$ K, and T_S is changed at initial time in the sensitivity experiments.

Although the experiment setup is idealized, it is able to reproduce the typical characteristics of squall lines, as detailed in the next section.

3. Basic characteristics and propagation of the squall line in the control simulation

a. Development of a mature squall line

Before investigating the effects of varying surface conditions on squall-line characteristics, we discuss the convection simulated in the control case scenario using $T_S = 300$ K. We focus here on the initial period that leads to the development of a mature squall line. In the following, we frequently refer to time after the start of the simulation t when discussing the characteristics of the simulation. Rain rates averaged over the analysis domain show that surface precipitation first occurs at $t = 30$ min (Fig. 2a) in association with the first storm. The time scale is comparable to that simulated in WK82 and similar idealized studies of deep convection (Seifert and Beheng 2006; Alfaro and Khairoutdinov 2015). The redevelopment of the first storm can be recognized by the second peak in domain-averaged rain rates by $t = 70$ min (Fig. 2a). The domain-mean rain rates produced from the first storm during the first roughly 120 min of the simulation are negligible. At the grid-point scale, however, these rain rates attain values of approximately 7.5 and 12 mm h^{-1} (not shown). The near-surface convective outflow of the first storm then interacts with the environmental wind shear, which leads to the development of a squall line. With the

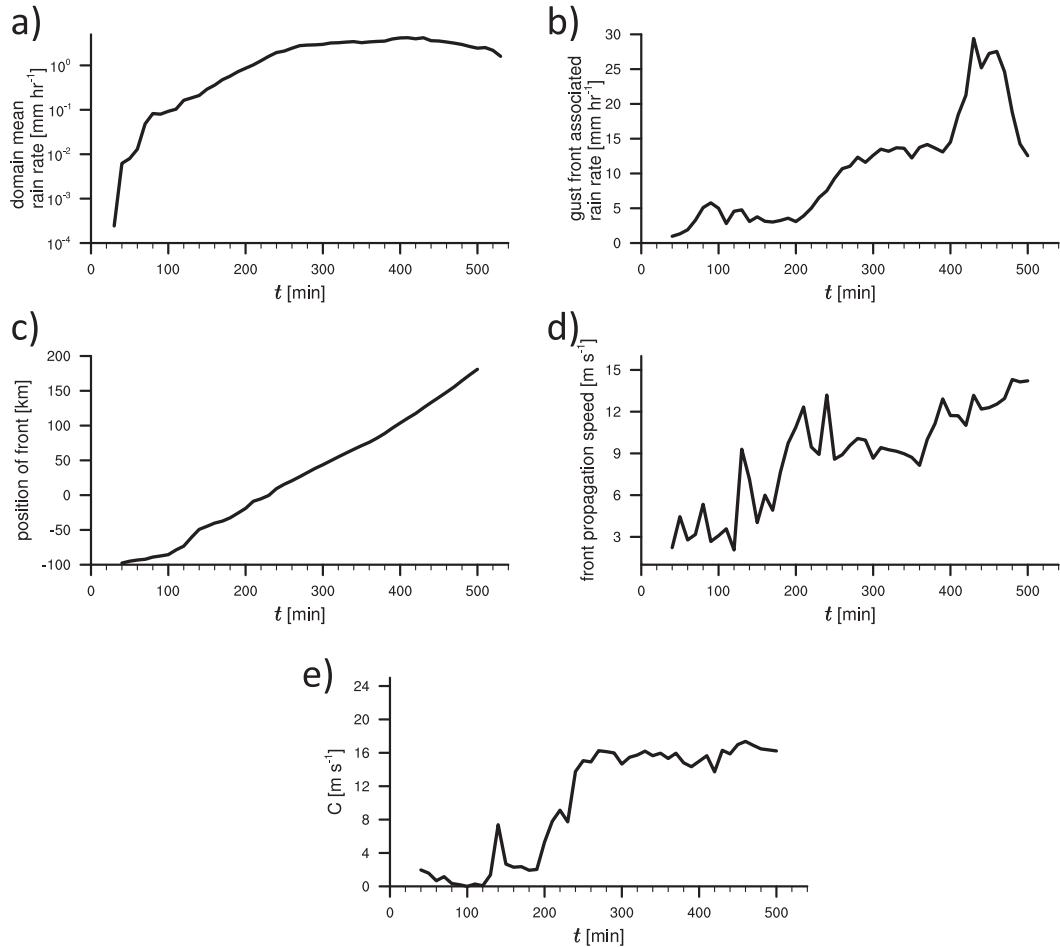


FIG. 2. Bulk characteristics of convection in the analysis domain. (a) Domain-mean rain rate (mm h^{-1}), (b) mean rain rate sampled in the vicinity of the cold pool edge (mm h^{-1}), (c) position of the front in the x direction (km), (d) propagation speed of front (m s^{-1}), and (e) theoretical cold pool propagation speed estimated from Eq. (2) (m s^{-1}). See main text for method of defining the front.

development of the squall line, domain-mean rain rate increases and remains at a relatively stable level of about 4 mm h^{-1} for $t \approx 250\text{--}450 \text{ min}$.

The primary interest of this study is on the characteristics of the propagating convective front. We track the position of the squall-line edge, or just “front” in the following, by associating it with the cold pool edge. We track the front following Bryan and Morrison (2012) and Grant and van den Heever (2016) by sampling for maxima in the horizontal gradient of near-surface (10 m above surface; i.e., the first model level) temperature $\Delta T_{10\text{m}}$. We calculate $\Delta T_{10\text{m}}$ over a distance of 6 km, where

$$\Delta T_{10\text{m}}(x, y) = T_{10\text{m}}(x + 6 \text{ km}, y) - T_{10\text{m}}(x, y). \quad (1)$$

We define the location of the front at every output time step and discrete y position, spaced 1 km apart, as the

most positive location in the x direction where $\Delta T_{10\text{m}}$ exceeds a threshold value γ , which is also within $+20 \text{ km}$ in the x direction of the front at the previous output time step. The second condition is necessary to avoid misidentification of the front due to convective cells developing ahead of the front (see section 3b). Also, it is unlikely that the front would advance by more than 20 km between two analysis time steps (10 min apart) as this would imply a propagation speed of roughly 33 m s^{-1} . Prior to computing along-line averages of the quantities of interest, the data are recentered on the location of the front over all y points. The results are therefore truly “front centered,” which reduces the effect of along-line variability.

Because $\Delta T_{10\text{m}}$ is not very large for the times where the squall line is not fully developed, we set the values of γ as follows: $\gamma = 0.1 \text{ K}$ for $0 < t \leq 150 \text{ min}$, 0.2 K for $160 \leq t \leq 200 \text{ min}$, and 0.3 K for $210 \leq t \leq 230 \text{ min}$. For

$t \geq 240$ min (i.e., for the well-developed squall line), $\gamma = 1.5$ K. The arguably very low values of γ for $t \leq 230$ min were chosen to obtain a large-enough sample size because the near-surface temperature perturbation ΔT_{10m} is small during the first hours of simulation. The initial storm (surface rainfall at $t = 30$ min; Fig. 2a) can however still not be identified in the near-surface temperature field (Fig. 2b). Visual comparisons of horizontal cross sections of the domain and the position of the front shown in Fig. 2c confirm the applicability of our tracking algorithm.

We show the resulting average rain rates in the vicinity of the front in Fig. 2b, where the vicinity is defined as the area covering 30 km behind the front and 10 km ahead of the front in the x direction (across line) to capture the evolution of surface precipitation in accordance with the different states of squall-line development (Rotunno et al. 1988). Between $t \approx 60$ and 100 min, the initial storm features average rain rates of up to about 5 mm h^{-1} (Fig. 2b). After the decay of the initial storm, surface precipitation in the vicinity of the front begins to build up from $t \approx 200$ min with the development of the squall line and attains a nearly constant surface rain rate of about 14 mm h^{-1} for $t \approx 250$ –380 min. The determined surface rain rates in the vicinity of the front compare well to those in earlier modeling studies [e.g., Fovell and Dailey (1995), their Fig. 10] and are on the lower end of observations of precipitation in the main convective region of squall lines, which reported values broadly in the range of 10 – 70 mm h^{-1} (Johnson and Hamilton 1988; Pereira Filho et al. 2002; Uijlenhoet et al. 2003; Chong 2010; Chen et al. 2016).

The increase in surface rain rates after the decay of the initial storm goes in hand with a significant acceleration of the cold pool propagation speed after $t \approx 180$ min (Figs. 2c,d). This increase in cold pool propagation speed is most probably associated with (i) an increase in cold pool strength due to increased evaporation and precipitation loading and (ii) the increased transport of higher-momentum air from aloft into near-surface layers with increasing intensity of the squall line [as explained in Mahoney et al. (2009)]. In Fig. 2e, we show a measure of the cold pool strength, namely, the theoretical speed of a density current C (Benjamin 1968), where

$$C^2 = 2 \int_0^H (-B) dz, \quad (2)$$

with B the buoyancy with respect to the prefrontal environment at every output interval and H the top of the cold pool, that is, the point where B first becomes positive sampling from the surface upward. The environment is defined as the area 5–10 km ahead of the front and the cold pool as the area 0–30 km behind the front.

Indeed, C increases markedly from $t \approx 200$ min onward and then stays approximately constant for $t > 250$ min. The propagation speed of the front is also fairly constant from $t \approx 250$ to 360 min ($\approx 10 \text{ m s}^{-1}$; Fig. 2d) and is within the range of observed (10 – 17 m s^{-1} ; Zipser 1977; Ogura and Liou 1980; Smull and Jr. 1985; Roux 1988; Redelsperger et al. 2000; Pereira Filho et al. 2002) but more at the low end of modeled squall-line propagation speeds (from 4.7 to $>20 \text{ m s}^{-1}$; Fovell and Ogura 1989; Fovell and Dailey 1995; Parker 2008; Alfaro and Khairoutdinov 2015; Alfaro 2017).

We illustrate the structure of the mature squall line at $t = 330$ min in Fig. 3. The corresponding horizontal cross section of vertical velocity at 1-km height is shown in Fig. 4a. Note that Fig. 4 utilizes an extended y axis to illustrate the inhomogeneity of convection in the y direction. The system-relative x -directional airflow (the difference between the front propagation speed and the domain wind) and the vertical velocity fields (Fig. 3a) show the characteristic features of a squall line: system-relative inflow at midlevels, marked gust front, strong near-surface winds in the cold pool, jump updraft, overturning updraft, ascending front-to-rear airflow, and descending rear flow in the stratiform precipitation region [Houze (2014) and references therein]. The cold pool shows a depth of 1 km, with near-surface θ_v perturbations in excess of -5 K (Fig. 3b). The increase in near-surface θ_v ahead of the squall line with respect to the initial conditions (Fig. 3b) results from the interactive surface fluxes and illustrates the transient character of near-surface environmental properties in our simulation setup. The distribution of cloud condensate (cloud water, cloud ice, and snow) and rainwater (Fig. 3c) also shows the characteristic features of a squall line. The anvil extends up to 70 km ahead of the front, the highest cloud condensate concentrations are simulated in the main convective region close to the front, and the trailing stratiform region is also very well established. Highest concentrations of rainwater reach the surface about 10 km behind the front and the trailing stratiform region is characterized by weaker surface precipitation (Fig. 3c).

We have thus confirmed that our simulation setup indeed enables us to simulate a well-developed, steady-state squall line with ICON from $t \approx 250$ min. The interactive surface fluxes act to modify the PBL air in our simulations (Fig. 3b)—the effect of which manifests itself later in the simulation and will be investigated next.

b. Initiation of prefrontal convection, discrete propagation, and squall-line acceleration

We have discussed that the simulated squall line shows equilibrium behavior, characterized by approximately

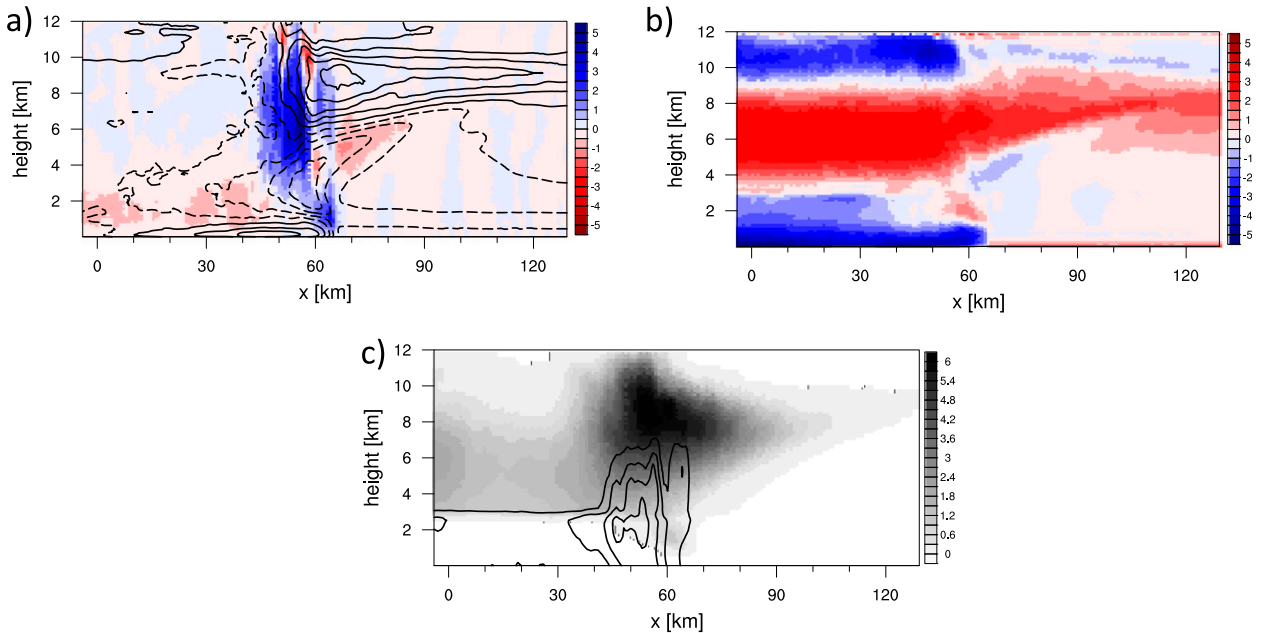


FIG. 3. Vertical cross sections of the well-developed squall line at $t = 330$ min in the control simulation. (a) Vertical wind (m s^{-1} ; shading) and system-relative x -directional wind (m s^{-1} ; contours every 3 m s^{-1} ; negative dashed), (b) $\Delta\theta_v$ perturbation with respect to the initial conditions (K), and (c) cloud condensate (g kg^{-1} ; shading) and rainwater mixing ratios (g kg^{-1} ; contours every 0.35 g kg^{-1} starting from 0.1 g kg^{-1}). Distance is given with respect to the center of the model domain. Properties averaged in the y direction of the analysis subdomain.

constant rain rates and gust-front propagation speed with time (Fig. 2) after $t = 250$ min. In the control simulation discussed here, the squall line is in this steady state until $t = 360$ min. At that time, the propagation speed increases by about 3 m s^{-1} (about 30% faster than before; Figs. 2c,d)

and approximately remains at that new level for the rest of the simulation. This increase occurs concurrently with the triggering of deep convection ahead of the squall line (Fig. 4b). The spatial pattern of this convection appears parallel to the front (Figs. 4b,c) and is associated

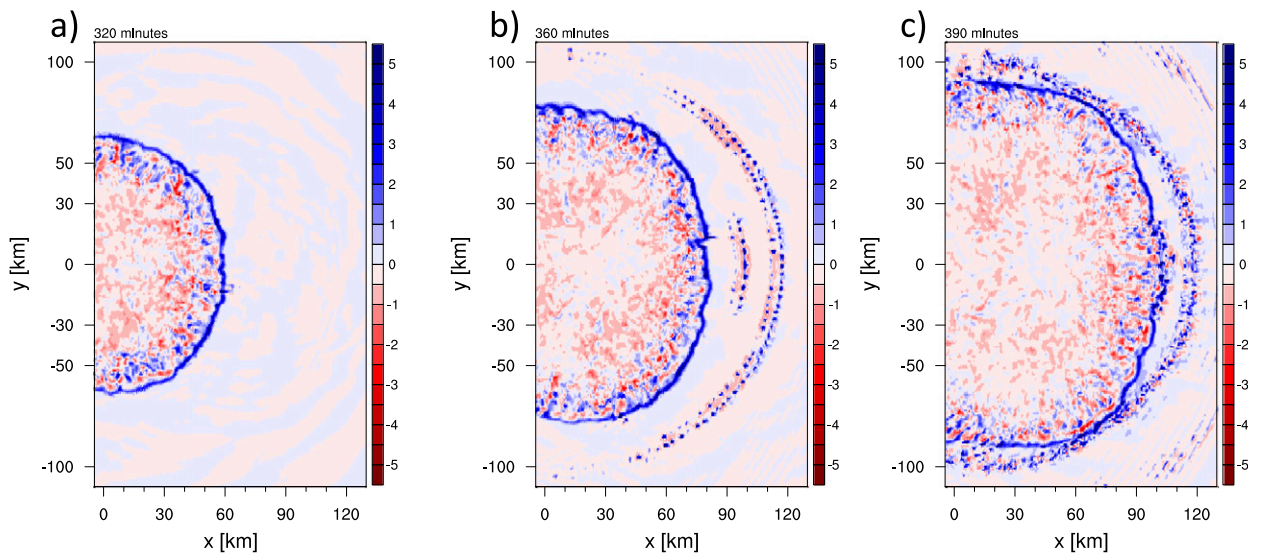


FIG. 4. Vertical wind (m s^{-1}) averaged from the surface to 2 km above the surface at $t =$ (a) 330, (b) 360, and (c) 390 min in the control simulation. The x and y distances are given with respect to the center of the model domain.

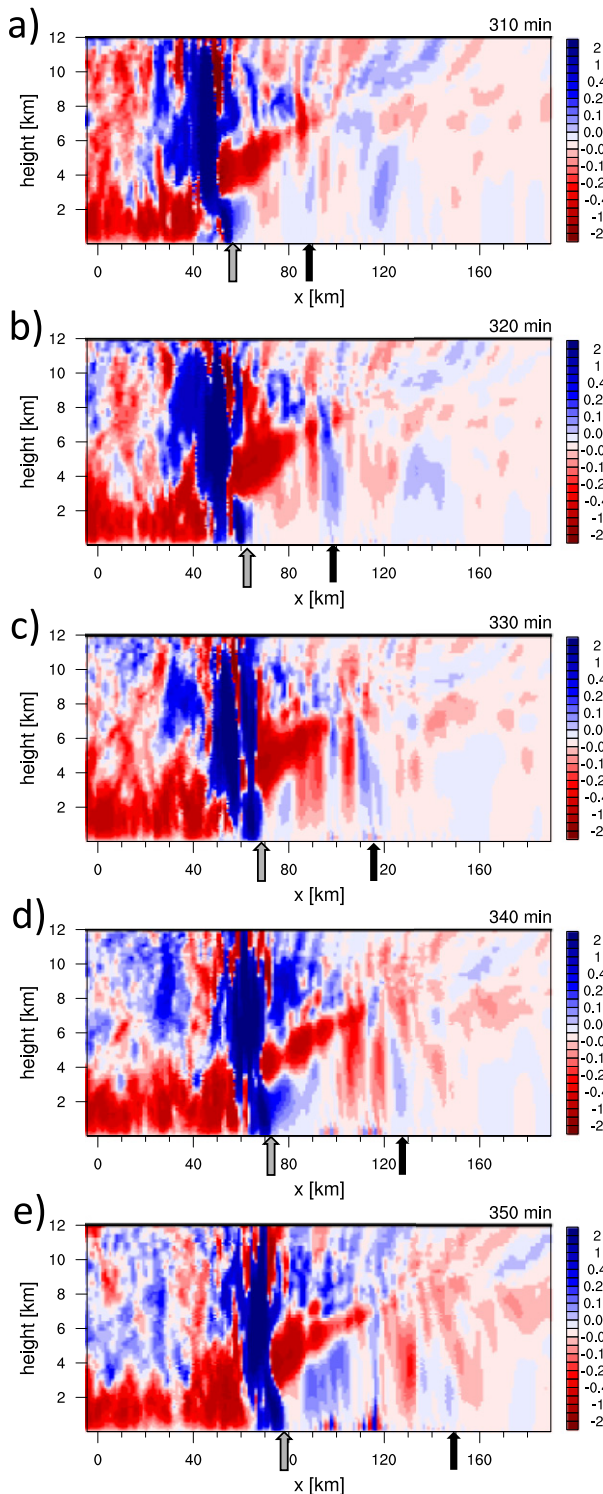


FIG. 5. Vertical cross sections of vertical wind (m s^{-1}) from $t =$ (a) 310 to (e) 350 min in the control simulation averaged in the y direction for $y \in [-15, 15]$ km. Black arrows track the location of one particular gravity wave envelope. Gray arrows track the location of the squall line.

with gravity waves excited by latent heating in the deep convection of the squall line. For illustrative purposes, we show vertical cross sections of vertical wind averaged in y direction ($y \in [-15, 15]$ km) for $t = 310$ – 350 min in Fig. 5. These gravity waves emanate away from the convective front in the free troposphere with a maximum amplitude near 5-km height (Fig. 5; cf. Fovell et al. 2006) and induce heterogeneous small-scale, 500–700-m-deep vertical motions in the PBL (Fig. 5c). These heterogeneities get amplified by succeeding gravity waves (Fig. 5d) and are eventually strong enough to result in the triggering of deep convection ahead of the front (Fig. 5e). Such convective initiation (or “secondary initiation,” denoted SI in the following) ahead of convective storms has been shown to occur in observations (e.g., Houze 1977; Grady and Verlinde 1997; Morcrette et al. 2006) and in idealized cloud-resolving model simulations (e.g., Fovell et al. 2006; Marsham and Parker 2006). As is evident from Fig. 4c, further SI also occurs at $t > 360$ min.

The appearance of convection ahead of the squall line may induce a discrete jump in the location of the gust front—a phenomenon called discrete propagation (e.g., Zipser 1977; Houze 1977; Carbone et al. 1990; Grady and Verlinde 1997; Fovell et al. 2006)—resulting in an acceleration of the squall line. After the occurrence of discrete propagation, squall-line propagation speed may slow down again but it remains higher than before the discrete propagation event (Fovell et al. 2006, their Figs. 2 and 15). A similar behavior can be depicted from Fig. 2d with the front propagation speed decreasing again slightly after $t = 390$ min. Rotunno et al. (1988) provide a possible first-order explanation for this sustained increase in propagation speed: in sheared environments in which the strength of the cold pool C exceeds the magnitude of the lower-tropospheric wind shear as in our simulations (section 4), a decrease in wind shear leads to an increase of cold pool propagation speed given the cold pool strength remains constant [Rotunno et al. (1988), their Eq. (12)]. In the case of discrete propagation, the prefrontal convection could indeed alter the wind shear profile ahead of the front, which could possibly feed back on the front propagation speed. We shed light on this possible connection in section 4.

The surface rain rates in the vicinity of the front also increase markedly (Fig. 2b) after the occurrence of SI, in agreement with Fovell et al. (2006) who found that discrete propagation can lead to an intensification of the squall line if the convective cells resulting from the SI are not too well developed compared to the squall

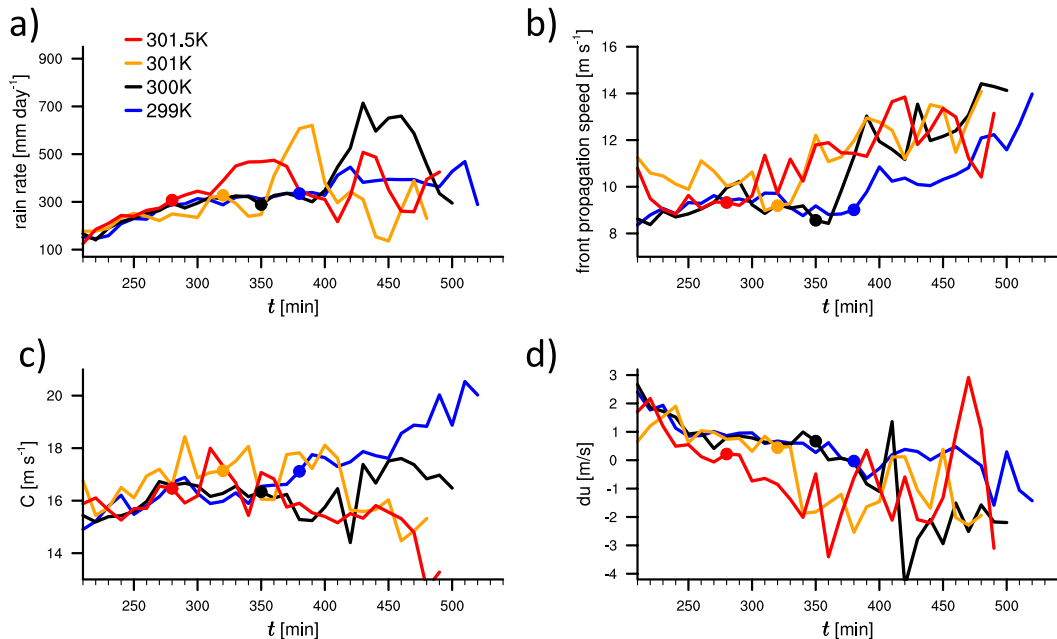


FIG. 6. Along-line average properties in the vicinity of the gust front of the well-developed squall lines in experiments with different T_S . (a) Surface rain rate averaged for the area from 30 km behind the front to 10 km ahead of the front (mm h^{-1}), (b) front propagation speed (m s^{-1}), (c) theoretical cold pool propagation speed estimated from Eq. (2) (m s^{-1}), and (d) wind shear Δu calculated over the depth of the cold pool H . Colored circles denote t_{ST} in each simulation. See main text for details.

line; otherwise their own cold pools could supplant the original squall line.

4. Simulations with varying surface conditions

To investigate the impact of varying surface temperature on the properties of the simulated squall line, we conduct additional experiments with differing T_S . Additional to the control simulation, we simulated the same WK82 test case with $T_S = 299, 301,$ and 301.5 K . We focus the analysis on the squall-line properties from the time at which the squall lines are well developed and have reached their first quasi-steady state.

All four simulations show similar rain rates in the vicinity of the front in their mature stage (Fig. 6a) until $t \approx 300$ min. The same holds for the corresponding front propagation speeds (Fig. 6b). Squall-line kinematics and precipitation strongly depend on the thermodynamics properties of the middle and upper troposphere (e.g., Takemi 2007; Houze 2014; Alfaro and Khairoutdinov 2015). We use the same initial conditions in all our simulations—the similarity among the simulated squall lines in their quasi-steady state is therefore not entirely unexpected. However, and as hypothesized in the introduction, changes in surface temperature and hence surface heat fluxes could have affected the properties of

the cold pool (Del Genio et al. 2012; Gentine et al. 2016; Grant and van den Heever 2016), which would have the potential to feed back on the squall line (Trier et al. 1996). To better assess this effect, we show in Fig. 6c a measure of the cold pool strength, namely, the theoretical speed of a density current C [Eq. (2)]. Although C can be interpreted as the theoretical propagation speed of a cold pool, it may only fully determine the propagation speed of a squall line as long as the low-level wind shear Δu does not vary [cf. Rotunno et al. (1988), their Eqs. (12)–(14)].

Like surface rain rates and front propagation speeds, C is also very similar among the simulations during the quasi-steady state of the squall lines up to $t = 300$ min. The cold pool strength seems unaffected by the surface fluxes, in contrast to Gentine et al. (2016) and Grant and van den Heever (2016), although the surface fluxes are of comparable magnitude or even higher than in those studies (not shown). That the cold pool strength calculated in the vicinity of the front in our simulations seems unaffected by the surface fluxes is related to the fact that in our simulations the cold pool is constantly fed by deep convective downdrafts. In such a case, convective cold pool strength strongly depends on the thermodynamic properties of the middle troposphere (e.g., Takemi 2007; Schlemmer and Hohenegger 2014; Alfaro and

Khairoutdinov 2015), which are identical in our simulations.

In contrast to this period of similarity among the simulations, the time evolution of surface rain rates and propagation speed begin to differ between the simulations after $t = 300$ min. This is due to differing times of SI ahead of the front. All of the sensitivity experiments feature SI ahead of the front at some point, the time of which, denoted t_{SI} , is indicated by the markers in Fig. 6. In all cases, surface rain rates in the vicinity of the front increase at or shortly after t_{SI} and propagation speed increases. We note that t_{SI} varies with T_S , with the warmest (coldest) simulation showing the earliest (latest) t_{SI} . This hints at a systematic relationship between the applied surface temperature, the associated modification of the near-surface air due to the altered surface fluxes, the occurrence of prefrontal deep convection, and the front propagation speed. We quantify this relationship in section 5.

The acceleration of the propagation speed (Fig. 6b) connects very well with t_{SI} and not with changes in cold pool properties anymore, as C remains similar among the simulations up to $t \approx 400$ min, which is well after t_{SI} . Once accelerated, the propagation speeds end up being similar although the evolutions of C among the simulations begin to diverge after $t \approx 360$ min: C decreases in time for the simulations with $T_S = 301$ and 301.5 K and increases for the other simulations. These different evolutions of C in the course of the simulations are associated with the strength of prefrontal convection and the associated influence on the near-surface air. With increasing T_S , prefrontal convection becomes more intense and widespread, resulting in a cooling of the prefrontal lower-tropospheric air due to evaporatively driven convective downdrafts. This is especially true for the simulations with $T_S = 301$ and 301.5 K where the prefrontal near-surface air temperature is up to 1 K lower than before the occurrence of SI (not shown). Because C is determined with respect to the prefrontal environment, the buoyancy profile becomes less negative and hence the cold pool weakens with time. The effect is also visible for the control simulation ($T_S = 300$ K), albeit not as pronounced. For the simulation with $T_S = 299$ K, however, the prefrontal convection is not as strong as in the other simulations, which results in a constant increase in prefrontal air temperatures with time and the corresponding increase in C .

Given the mismatch between C and front propagation speed, how can the acceleration of the front from t_{SI} be understood? In fact, Rotunno et al. (1988) provide the basis for a simple answer. They showed that in sheared environments, front propagation speed depends on the ratio of cold pool strength C to lower-tropospheric wind shear Δu [cf. their Eqs. (12)–(14)]. In situations where

$C > \Delta u$, a decrease in Δu leads to an increase in front propagation speed as long as C remains constant [Rotunno et al. (1988), their Eq. (12)]. To shed light on this behavior, we show the temporal evolution of Δu , calculated over the depth of the cold pool H in the area 5–10 km ahead of the front, in Fig. 6d. The value of Δu actually slowly decreases with time due to turbulent mixing near the surface but stays relatively constant during the period where the squall lines are well established from $t \approx 250$ min up to t_{SI} . At $t \approx t_{\text{SI}}$, Δu decreases markedly in all simulations (except for the one with $T_S = 299$ K), which connects to the increase in front propagation speed given constant C .

We attribute the changes in lower-tropospheric wind shear to the appearance of secondary convection ahead of the front. To support our conjecture, we show horizontal and vertical cross sections of u wind (m s^{-1}) for simulation times t centered around the initiation of secondary convection in the control simulation ($T_S = 300$ K, $t_{\text{SI}} = 350$ min) in Fig. 7. It is interesting to note that prefrontal wind speed in the lowermost levels is negative in x direction, thereby constituting an inflow into the convective system (Fig. 7a). From t_{SI} onward, the low-level wind speed close to the edge of the original front shows positive values at the locations of SI (about 95 and 110 km; Figs. 7b,c). This suggests downward transport of horizontal momentum to the lower troposphere by the secondary convection, which acts to reduce the wind shear over the depth of the original cold pool, supporting an increase in front propagation speed in accordance with Rotunno et al. (1988). Further, convection continues to be triggered ahead of the front for times $t > t_{\text{SI}}$ (Fig. 4c), which explains the large variability of Δu in Fig. 6d. Although the simulated effects on front propagation speed and the key features of the simulations agree well with the simple theoretical perspective given in Rotunno et al. (1988), other mechanisms may also play a role. First, discrete propagation (i.e., the acceleration of the original convective front) is commonly associated with the merging of the original with the secondary convection (cf. Fig. 4c). Near-surface air temperature indicates that the original cold pool indeed bulges out toward the secondary convection at $t = 390$ min in the control simulation (not shown). Second, the acceleration of the squall line could in part be due to effects of the secondary convection on the strength of the squall-line convection—a mechanism that has been shown to influence sea-breeze front propagation speeds (Fovell and Dailey 2001).

For the $T_S = 299$ -K simulation, the decrease in Δu is more subtle around $t \approx t_{\text{SI}}$. This is because the convection initiated ahead of the front in the $T_S = 299$ -K simulation is not as deep as that simulated in the other simulations (not shown), which reduces the impact on the environmental wind profile. It is just toward the end of the simulation

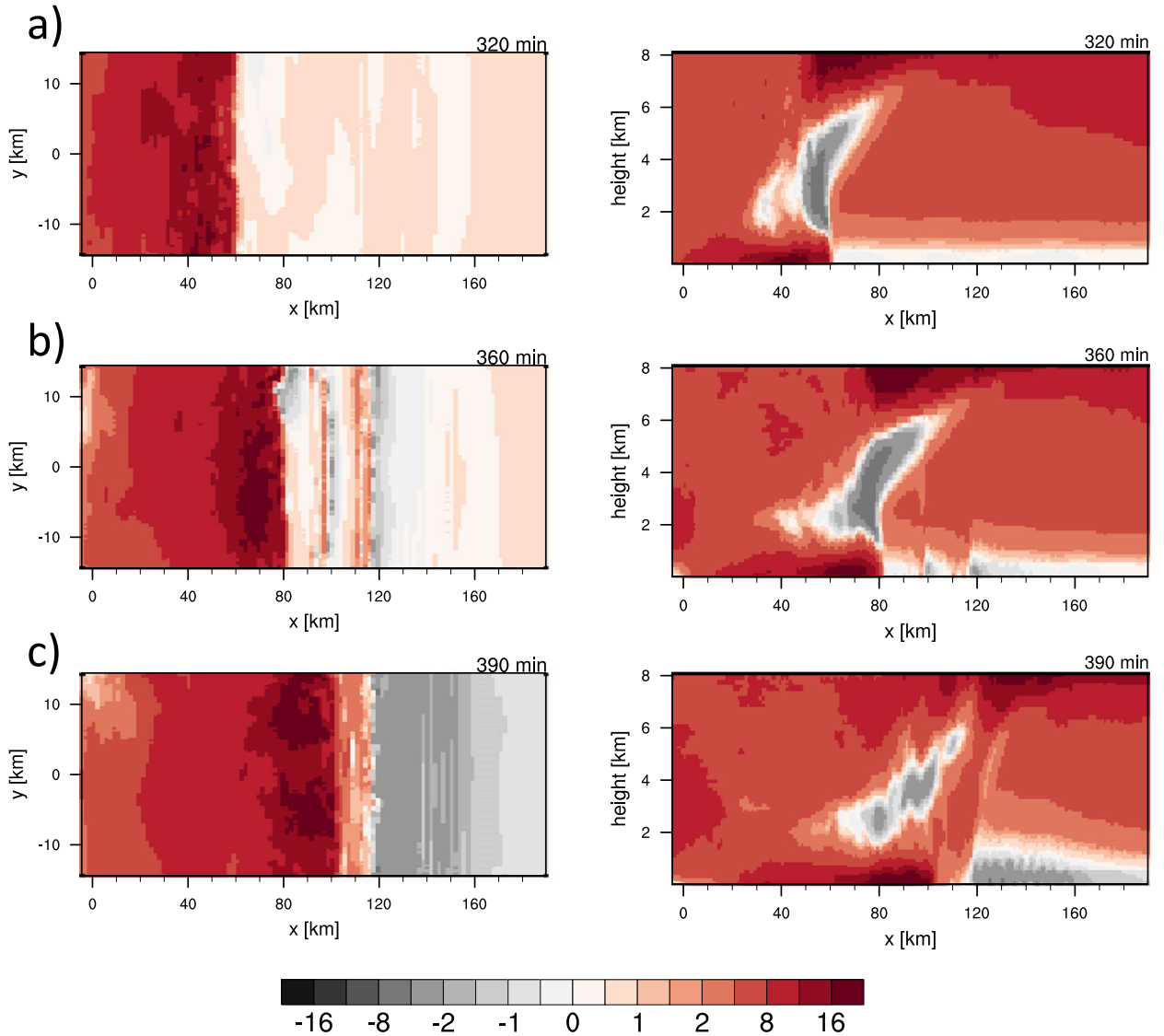


FIG. 7. (left) Horizontal and (right) vertical cross sections of u wind (m s^{-1}) in the control simulation ($\text{SST} = 300 \text{ K}$) for different simulation times $t =$ (a) 320, (b) 360, and (c) 390 min. The horizontal cross section shows averages at about 1-km height. Note the irregular spacing of the color scale.

around $t = 470 \text{ min}$ where the prefrontal convection is deep enough to have a pronounced impact on the environmental wind profile in the $T_S = 299\text{-K}$ simulation (Fig. 6d). The limited impact of the prefrontal convection on Δu in the $T_S = 299\text{-K}$ simulation also explains why the front propagates slower than in the other simulations despite the large values of C : the effect of the prefrontal convection on Δu in the warmer simulations trumps the increase in C in the colder simulation.

5. Surface flux preconditioning

In the foregoing section, we suggested that there exists a systematic relationship between the applied

surface temperature T_S , the associated modification of the near-surface air due to the altered surface fluxes and the time of prefrontal deep convection t_{SI} . Warmer T_S leads to earlier t_{SI} , suggesting a more effective preconditioning of the atmosphere toward the triggering of deep convection with increasing T_S . We quantify this suggested relationship in this section.

We show the surface buoyancy fluxes $B_0(t)$ for all simulations in Fig. 8a. We calculate $B_0(t)$ following Garratt (1992), where

$$B_0(t) = \frac{g}{\rho c_p T(t)} \left[\text{SHF}(t) + 0.61 \frac{c_p T(t)}{L} \text{LHF}(t) \right], \quad (3)$$

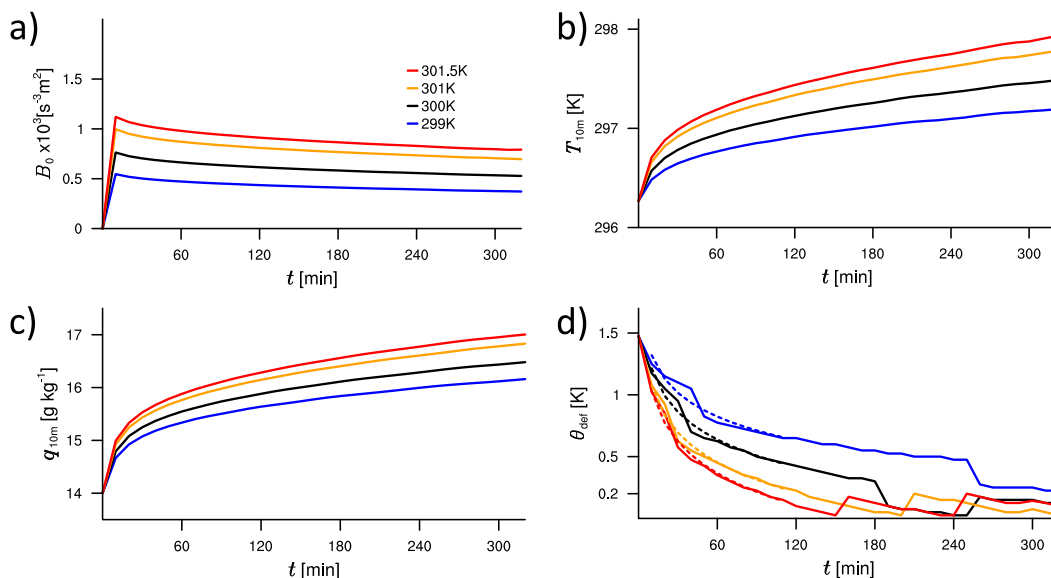


FIG. 8. Evolution of near-surface variables in a part of the model domain not influenced by the squall lines during the time period of analysis. (a) Surface buoyancy flux B_0 ($\text{m}^2 \text{s}^{-3}$), (b) air temperature (K), and (c) specific humidity (g kg^{-1}) in the lowest model level (10 m above surface), and (d) θ_{def} (K) calculated for every model output interval after T14. Dashed lines in (d) depict logarithmic fits following $\theta_{\text{def}}(t) = c_r + \lambda_{T_S} \ln t$ to the data. See main text for details.

with SHF and LHF the sensible and latent heat fluxes at the surface, T and ρ the air temperature and density at the surface, respectively, and L the latent heat of vaporization. SHF and LHF are available as model diagnostic output. We evaluate $B_0(t)$ for every grid point and then average in the y direction over the area from 190 to 195 km in the x direction—that is, at the right-most end of the subdomain used for the analysis of the squall-line properties. We chose this area for the analysis of the surface fluxes to avoid disturbances caused by the passing squall-line and/or secondary convection initiated ahead of the squall line. The same computation methodology also applies to all other diagnostics introduced in this section. As expected, $B_0(t)$ is highest (lowest) for the run with highest (lowest) T_S . Near-surface (lowest model level) temperature $T_{10\text{m}}$ and moisture $q_{10\text{m}}$ (Figs. 8b,c) change accordingly while the difference in $T_{10\text{m}}$ and $q_{10\text{m}}$ among the simulations stays approximately constant in time. As near-surface wind speeds are similar for all simulation, the differences in $B_0(t)$ result from the differences in T_S . The value of B_0 decreases with increasing simulation time t due to the constant boundary layer moistening and warming that reduces the near-surface gradients of temperature and moisture. It is more than evident that these changes in buoyancy flux due to changes in T_S will affect the initiation of convection ahead of the squall line; the question is whether this can be predicted a priori. This would allow us to infer under which

conditions the surface is important for squall-line propagation.

To do so, we apply the recently introduced “heated condensation framework” (HCF; Tawfik and Dirmeyer 2014, hereafter T14). In short, the HCF can be applied to quantify the conditioning of the atmospheric column toward the initiation of deep convection due to buoyancy processes alone. The associated calculations only require knowledge of the atmospheric profiles of temperature and moisture. Given a particular atmospheric sounding, applying the HCF yields the near-surface potential temperature deficit θ_{def} or the near-surface moisture deficit q_{def} that need to be overcome to trigger convection. These parameters are derived by calculating hypothetical mixed layers by combining adiabatic ascents with increasingly warmer near-surface air parcels with the environmental profile (see T14 for details). Then, θ_{def} corresponds to the amount the near-surface potential temperature needs to increase in order to increase the height of the hypothetical near-surface mixed layer so as to attain saturation at the top. In this instance, the atmosphere is seen as preconditioned toward the triggering of deep convection (T14). On the other hand, q_{def} can be seen as the additional moisture needed in the mixed layer to attain saturation at its top without increasing its height and thus allow for the triggering of deep convection.

We apply the HCF in favor of more common approaches relying on parcel-based frameworks like the

lifting condensation level (LCL), the level of free convection (LFC), or the convective inhibition (CIN) to estimate the preconditioning of the atmosphere because these typically neglect the incremental growth of the PBL and depend on the properties of the parcel selected for lifting (cf. T14 for details).

We calculate θ_{def} and q_{def} for every model output time step. T14 suggested using values of temperature and moisture at 2 m above the surface for applying the HCF framework. The ICON model does not provide those values; we therefore use the values of temperature and moisture in the middle of the lowest model level, $T_{10\text{m}}$ and $q_{10\text{m}}$, respectively.

As the initial sounding for the WK82 test case resembles a very unstable environment, the values of θ_{def} are very low and identical for all simulations at their start (Fig. 8d). This indicates that very little heating of the near-surface air is needed to precondition the atmospheric column for deep convection. The value of θ_{def} decreases with t in all simulations owing to the continuous heating by surface fluxes and reach close to zero except in the $T_S = 299\text{-K}$ simulation. More importantly the decrease in θ_{def} is faster with larger B_0 and hence in the simulations starting with warmer T_S . Calculations of q_{def} also show decreasing values during the first $t = 0\text{--}40$ min of simulation time; q_{def} then remains approximately constant and the values do not converge among the simulations (not shown). Hence it seems that the tested atmospheric sounding is more efficaciously preconditioned by decreases in θ_{def} than q_{def} . Employing a different atmospheric sounding—for example, a drier one—would most probably lead to different results.

The discontinuous jumps in θ_{def} —for example, at $t = 150$ min for the 301.5-K simulation—result from the discretization of the model's vertical grid and are associated with the change in the height of the saturation level.

6. Metrics to estimate t_{SI}

Given the systematic relationship between the evolution of θ_{def} and B_0 , we aim at devising a simple quantitative relationship to estimate t_{SI} given an atmospheric sounding and estimates of B_0 . The evolution of θ_{def} during the first 2 h of simulation in Fig. 8d indicates that the decay rate of θ_{def} might provide some predictive skill for the onset of SI. This is estimated by the metric

$$M_1^{\text{SI}}(T_S) = \lambda_{T_S}, \quad (4)$$

where λ_{T_S} is the decay rate (K min^{-1}) as estimated from logarithmic fits to $\theta_{\text{def}}(t)$ (dashed lines in Fig. 8d). We show t_{SI} as function of M_1^{SI} in Fig. 9a and this indeed

reveals a systematic dependence of t_{SI} on M_1^{SI} , with smaller values, and hence a faster reduction of θ_{def} , resulting in sooner SI. Although the relationship between M_1^{SI} and t_{SI} is systematic (Fig. 9a), applying M_1^{SI} in an operational setting is difficult as this requires knowledge of λ_{T_S} . The relationship is also implicitly only dependent on T_S and therefore neglects effects of surface moisture.

As an alternate formulation, we thus devise a metric $M_2^{\text{SI}}(t)$, which relates the difference in θ_{def} at a point during the simulation $\theta_{\text{def}}(t)$ and its minimum value $\theta_{\text{def,min}}$ to the surface buoyancy flux at that time $B_0(t)$ such that

$$M_2^{\text{SI}}(t) = \frac{\Delta\theta_{\text{def}}(t)}{B_0(t)}, \quad \Delta\theta_{\text{def}}(t) = \theta_{\text{def}}(t) - \theta_{\text{def,min}}. \quad (5)$$

Thus, $M_2^{\text{SI}}(t)$ relates the value $\Delta\theta_{\text{def}}(t)$ to the available heat input at the surface $B_0(t)$, which acts to reduce $\Delta\theta_{\text{def}}(t)$ through heating and moistening. We show the relationship between $M_2^{\text{SI}}(t)$ and t_{SI} for $t = 10$ min in Fig. 9b, where the values denoted by black markers are calculated using the actual values of $\theta_{\text{def,min}}$ attained during the simulations. For the $T_S = 299\text{-K}$ simulation we use $\theta_{\text{def,min}} = \theta_{\text{def}}(380 \text{ min}) = 0.18 \text{ K}$ and not the actual value of $\theta_{\text{def,min}} = 0.1 \text{ K}$, which was attained after SI had occurred. The values denoted by red markers in Fig. 9b were derived using an assumed value of $\theta_{\text{def,min}} = 0.2 \text{ K}$ to avoid a priori knowledge of the value of $\theta_{\text{def,min}}$. In an operational setting, $B_0(t)$ could be estimated from a previous time or from climatology. Given the inherent uncertainties in the estimation of M_2^{SI} , the functional dependence $t_{\text{SI}}(M_2^{\text{SI}})$ is simply approximated by a linear regression. As shown in Fig. 9b, this simple fit still gives a very good agreement with the actual values. The linear relationship appears to break down for small values of M_2^{SI} , though.

To test the validity of the proposed relationship with respect to our initial sounding, we rerun the $T_S = 300\text{-K}$ simulation starting from a slightly less unstable initial sounding with $q_{v,\text{max}} = 13 \text{ g kg}^{-1}$. The corresponding asterisks in Fig. 9 approximately fall on the previously derived relationships between t_{SI} and $M_{1,2}^{\text{SI}}$ confirming the potential usefulness of these relationships.

We can use the linear relationship between M_2^{SI} and t_{SI} indicated by the red line in Fig. 9b to predict the change in T_S needed to achieve a change in the time of SI, Δt_{SI} , and hence affect the squall-line propagation. To do so, we use the linear dependence of B_0 on T_S as obtained from our simulations (see appendix for details). In Fig. 10, we show the values of ΔT_S needed to achieve a range of values of Δt_{SI} given environmental values of θ_{def} . The value of Δt_{SI} is given with respect to the occurrence of SI at $t = 360$ min (cf. appendix), with more

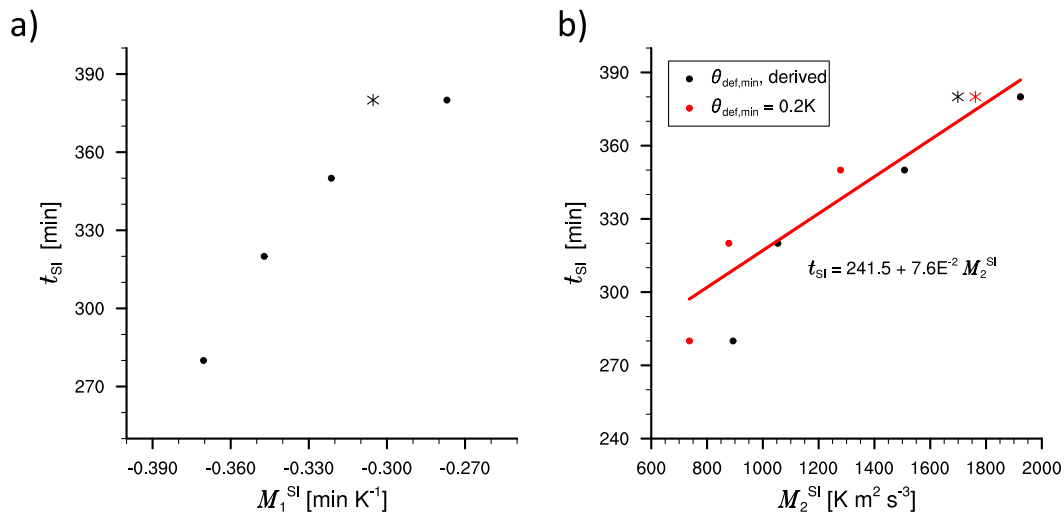


FIG. 9. Functional dependence of t_{SI} on (a) M_1^{SI} and (b) M_2^{SI} calculated from Eqs. (4) and (5). Dots indicate values calculated from the simulations applying $q_{v,\text{max}} = 14 \text{ g kg}^{-1}$ discussed in section 4. Asterisks indicate values derived from a simulation performed with $q_{v,\text{max}} = 13 \text{ g kg}^{-1}$ and $T_S = 300 \text{ K}$. Black markers in (b) show values using the actual value of $\theta_{\text{def,min}}$ attained during the simulations; red markers denote values obtained when assuming $\theta_{\text{def,min}} = 0.2 \text{ K}$. The linear regression (red line) in (b) approximates $t_{\text{SI}}(M_2^{\text{SI}})_{\theta_{\text{def,min}}=0.2\text{K}}$ and is given by the equation in (b). See main text for details.

negative values of Δt_{SI} representing an earlier occurrence of SI. As expected, the value of ΔT_S increases with values of θ_{def} and an earlier occurrence of SI (more negative values of Δt_{SI}). During midlatitude summertime conditions, it is not uncommon for T_S to increase by more than 20 K between early morning and midday as a result of solar insolation. According to T14, values of θ_{def} can be larger than 25 K for the continental United States. Assuming ΔT_S of up to 20 K, a change in t_{SI} of 3 h and more would be possible under those conditions (Fig. 10). In already quite preconditioned regimes with values of θ_{def} of 8 K—for example, the southeastern United States in summer (T14)—a change in t_{SI} of 3 h would only require $\Delta T_S \approx 8 \text{ K}$, whereas a value of $\Delta T_S = 20 \text{ K}$ would lead to an earlier occurrence of SI by approximately 4.5 h. We note that the here-proposed relationships were derived from a limited set of environmental conditions. It would be interesting to prove these relationships not only in a larger number of cases [e.g., following the approach detailed in Letkewicz et al. (2013)] but also in observed settings. This is left for future work.

7. Summary and conclusions

We applied the unified ICON modeling system (Zängl et al. 2015) at cloud-system-resolving resolution (1 km) to study the effect of surface conditions on the characteristics of fully developed mesoscale convective systems. Specifically, we investigated the effect of varying

surface temperatures T_S on mature squall lines. We considered values of $T_S = 299, 300, 301,$ and 301.5 K . All these temperatures were higher than the air temperature of the lowest model level, leading to a constant heating and moistening of the boundary layer throughout the simulations.

The squall lines were initiated using the WK82 test-case setup in which a warm bubble perturbation first initiates an intense storm system that then dissipates. The squall lines we studied here then developed at the leading edge of the convective outflow of the initial storm system. The squall lines attained a mature state after approximately 4 h of simulation and featured the established dynamical and morphological characteristics of squall-line systems with trailing stratiform precipitation. Surface conditions had only a marginal impact on the squall-line properties during this part of the simulations as all squall lines showed similar rain rates and propagation speeds.

The model setup was chosen as to maximize the effect of surface fluxes on the environment and the convectively generated cold pool (fixed surface temperatures and latent heat flux computation assuming saturation with respect to water vapor at the surface). At the outset of this study, we assumed that one major pathway of surface fluxes to influence squall-line properties would be through modification of the cold pool strength, with higher T_S acting to reduce cold pool strength more effectively compared to lower T_S . However, we found no discernible impact of different values

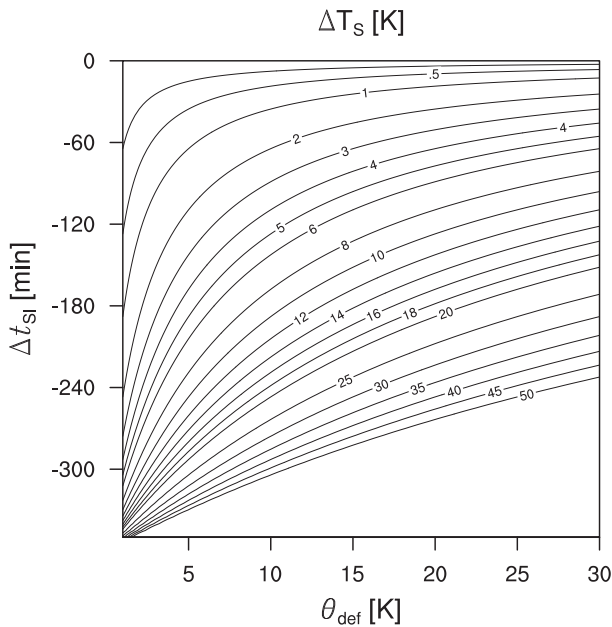


FIG. 10. Change in surface temperature ΔT_S (K) needed to change the timing of SI Δt_{SI} given a value of θ_{def} of the environmental profile. The functional relationship $\Delta T_S(\Delta t_{SI}, \theta_{def})$ is derived using the linear regression approximating $t_{SI}(M_2^{SI})_{\theta_{def, min}=0.2\text{K}}$ shown by the red line in Fig. 9b and the linear dependence of B_0 on T_S (see appendix). The minimum contour level is 0.2 K. Values of $\Delta T_S > 50$ K are not plotted. See main text for details.

chosen for T_S on the cold pool strength averaged over the area 30 km behind the squall-line front. This is because the convectively generated cold pool is constantly fed by downdraft air stemming from the middle troposphere, which the surface fluxes cannot counteract.

The only effect of the land surface was that the simulations showed initiation of secondary convection (SI) several tens of kilometers ahead of the front of the propagating squall line. From the time of SI t_{SI} , the simulations showed a systematic increase in the propagation speed of the well-established squall lines. Such a sudden increase in propagation speed after the occurrence of SI ahead of a squall line is known as discrete propagation (Zipser 1977; Grady and Verlinde 1997; Fovell et al. 2006). In our simulations, the propagation speed of the squall lines after SI remained higher than before—a phenomenon we attribute to a reduction of wind shear in the lowermost troposphere ahead of the squall line due to the occurrence of SI. The prefrontal deep convection acts to homogenize the environmental wind profile through downward mixing of higher-momentum air, thereby reducing the wind shear over the depth of the cold pool. The relationship between squall-line propagation speed, cold pool strength, and environmental wind shear is explained in

Rotunno et al. [1988, their Eqs. (12)–(14)]. They showed that in sheared environments in which the strength of the cold pool exceeds the magnitude of the lower-tropospheric wind shear as in our simulations (section 4), a decrease in wind shear leads to an increase of cold pool propagation speed given the cold pool strength remains constant [Rotunno et al. (1988), their Eq. (12)]. These relationships may not give the full picture regarding the propagation speed of the squall lines, but we believe that, as a first step, it makes sense to use a simple theory to understand what is happening and it seems that, in this case, the simple theory explains the key features of the simulation. A more detailed investigation of the exact mechanisms leading to the acceleration of the squall-line propagation is left for future work.

We found that t_{SI} shows a systematic relationship with T_S , with warmer T_S resulting in earlier t_{SI} suggesting a more rapid preconditioning of the atmospheric column toward the occurrence of deep convection compared to colder T_S .

We predict t_{SI} given environmental conditions by applying the heated condensation framework (HCF) introduced by T14. HCF allows to quantify the needed heating and moistening of the planetary boundary layer from surface fluxes to precondition the atmosphere toward the triggering of deep convection. In doing so, we found an approximately linear relationship between t_{SI} and the surface buoyancy flux B_0 , with larger values of B_0 resulting in a more rapid conditioning of the atmosphere toward deep convection. This resulted in an earlier onset of SI ahead of the squall line and thus in an earlier acceleration of the squall line. We used this linear relationship to devise a model allowing us to estimate the change in surface temperature ΔT_S needed to achieve a change in the onset time of SI Δt_{SI} given a wide range of environmental conditions. From that model, we found that the typical diurnal evolution of T_S can provide sufficient surface forcing to advance the occurrence of SI by up to 3 h.

The strongly idealized simulations we performed here of course only sample a small part of the possible environmental conditions in which squall lines and SI with the associated discrete propagation can occur. Specifically, we chose the upper and lower ends of the T_S range so that secondary convection does not occur before the squall line is fully developed and so that secondary convection does still occur within reasonable simulation time, respectively. Also, we note that the values of t_{SI} that we found here should be considered as conservative estimates because SI occurred much later (up to 2 h) than the time the atmosphere was conditioned toward deep convection. We associate this delay with the lack of inhomogeneity of surface conditions in our simulations

which would otherwise have led to much earlier SI. Decreasing the model grid spacing could also result in an earlier onset of SI (Petch et al. 2002). Further, in an operational setting, radiative processes such as heating of the surface would most probably lead to much earlier SI. However, we conjecture that the relationship between B_0 and t_{SI} does not deviate significantly from the linear relationship we found here (given the near-surface wind speed) if the abovementioned processes were taken into account. This is however out of the scope of the present study and will be quantified in future work.

Acknowledgments. We appreciate the very constructive feedback by three anonymous reviewers and the editor Robert Fovell, which significantly helped to improve the manuscript. We thank Christopher Moseley (MPI-M) for constructive comments on the pre-submission version of the manuscript. KP acknowledges funding by the BMVI (Federal Ministry of Transport and Digital Infrastructure) in the framework of the Hans-Ertel-Zentrum für Wetterforschung [Hans-Ertel-Zentrum for Weather Research (HERZ)]. HERZ is a research network of universities, research institutes, and the Deutscher Wetterdienst (DWD) funded by the BMVI. Use of the supercomputer facilities at the Deutsches Klimarechenzentrum (DKRZ) is acknowledged. The figures were created using NCAR (2014). Primary data and scripts used in the analysis and other supplementary information that may be useful in reproducing the author's work are archived by the Max Planck Institute for Meteorology and can be obtained by contacting publications@mpimet.mpg.de.

APPENDIX

The Model Linking Δt_{SI} to ΔT_S

The goal is to obtain a model that estimates the change in surface temperature ΔT_S needed to change the onset in timing of SI Δt_{SI} given a certain value of θ_{def} .

The linear approximation linking t_{SI} and M_2^{SI} given by the red line in Fig. 9b is given by

$$t_{\text{SI}}(M_2^{\text{SI}}) = c_M + b_M M_2^{\text{SI}}, \quad (\text{A1})$$

with $b_M = 7.56 \times 10^{-2} \text{ min s}^3 \text{ K}^{-1} \text{ m}^{-2}$ and $c_M = 241.5 \text{ min}$, and M_2^{SI} given by Eq. (5). From our simulations, we estimate $B_0(T_S)$ as

$$B_0(T_S) = c_{T_S} + b_{T_S} T_S, \quad (\text{A2})$$

with $c_{T_S} = -6.804 \times 10^{-2} \text{ m}^2 \text{ s}^{-3}$ and $b_{T_S} = 2.293 \times 10^{-4} \text{ m}^2 \text{ s}^{-3} \text{ K}^{-1}$. Combining the above two equations

with Eq. (5) and letting $c_M = 0$ (because we are only interested in changes and not absolute values), we obtain an expression for $T_S(t_{\text{SI}}, \Delta\theta_{\text{def}})$:

$$T_S(t_{\text{SI}}, \theta_{\text{def}}) = \frac{b_M \Delta\theta_{\text{def}}}{t_{\text{SI}} b_{T_S}} - \frac{c_M}{b_{T_S}}. \quad (\text{A3})$$

We estimate ΔT_S with respect to the occurrence of SI at $t_{\text{SI}} = 360 \text{ min}$, which we assume as the squall line's lifetime for reasons of simplicity, yielding

$$\Delta T_S(\Delta t_{\text{SI}}, \Delta\theta_{\text{def}}) = T_S(t_{\text{SI}}, \Delta\theta_{\text{def}}) - T_S(360 \text{ min}, \Delta\theta_{\text{def}}), \quad (\text{A4})$$

where $\Delta t_{\text{SI}} = 360 \text{ min} - t_{\text{SI}}$.

REFERENCES

- Adler, B., N. Kalthoff, and L. Gantner, 2011: The impact of soil moisture inhomogeneities on the modification of a mesoscale convective system: An idealised model study. *Atmos. Res.*, **101**, 354–372, doi:10.1016/j.atmosres.2011.03.013.
- Alfaro, D. A., 2017: Low-tropospheric shear in the structure of squall lines: Impacts on latent heating under layer-lifting ascent. *J. Atmos. Sci.*, **74**, 229–248, doi:10.1175/JAS-D-16-0168.1.
- , and M. Khairoutdinov, 2015: Thermodynamic constraints on the morphology of simulated midlatitude squall lines. *J. Atmos. Sci.*, **72**, 3116–3137, doi:10.1175/JAS-D-14-0295.1.
- Benjamin, T. B., 1968: Gravity currents and related phenomena. *J. Fluid Mech.*, **31**, 209–248, doi:10.1017/S0022112068000133.
- Betts, A. K., and C. Jakob, 2002: Study of diurnal cycle of convective precipitation over Amazonia using a single column model. *J. Geophys. Res.*, **107**, 4732, doi:10.1029/2002JD002264.
- Bryan, G. H., and H. Morrison, 2012: Sensitivity of a simulated squall line to horizontal resolution and parameterization of microphysics. *Mon. Wea. Rev.*, **140**, 202–225, doi:10.1175/MWR-D-11-00046.1.
- , J. C. Wyngaard, and J. M. Fritsch, 2003: Resolution requirements for the simulation of deep moist convection. *Mon. Wea. Rev.*, **131**, 2394–2416, doi:10.1175/1520-0493(2003)131<2394:RRFTSO>2.0.CO;2.
- Carbone, R. E., J. W. Conway, N. A. Crook, and M. W. Moncrieff, 1990: The generation and propagation of a nocturnal squall line. Part I: Observations and implications for mesoscale predictability. *Mon. Wea. Rev.*, **118**, 26–49, doi:10.1175/1520-0493(1990)118<0026:TGAPOA>2.0.CO;2.
- Chen, B., J. Wang, and D. Gong, 2016: Raindrop size distribution in a midlatitude continental squall line measured by Thies optical disdrometers over east China. *J. Appl. Meteor. Climatol.*, **55**, 621–634, doi:10.1175/JAMC-D-15-0127.1.
- Chong, M., 2010: The 11 August 2006 squall-line system as observed from MIT Doppler radar during the AMMA SOP. *Quart. J. Roy. Meteor. Soc.*, **136**, 209–226, doi:10.1002/qj.466.
- Clark, D. B., C. M. Taylor, and A. J. Thorpe, 2004: Feedback between the land surface and rainfall at convective length scales. *J. Hydrometeorol.*, **5**, 625–639, doi:10.1175/1525-7541(2004)005<0625:FBTLA>2.0.CO;2.
- Del Genio, A. D., J. Wu, and Y. Chen, 2012: Characteristics of mesoscale organization in WRF simulations of convection

- during TWP-ICE. *J. Climate*, **25**, 5666–5688, doi:10.1175/JCLI-D-11-00422.1.
- Dipankar, A., B. Stevens, R. Heinze, C. Moseley, G. Zängl, M. Giorgetta, and S. Brdar, 2015: Large eddy simulation using the general circulation model ICON. *J. Adv. Model. Earth Syst.*, **7**, 963–986, doi:10.1002/2015MS000431.
- Doms, G., and Coauthors, 2011: A description of the nonhydrostatic regional COSMO model—Part II: Physical parameterization. Consortium for Small-Scale Modelling LM_F90 4.20, 154 pp. [Available online at <http://www.cosmo-model.org/content/model/documentation/core/cosmoPhysParamtr.pdf>.]
- Fovell, R. G., and Y. Ogura, 1989: Effect of vertical wind shear on numerically simulated multicell storm structure. *J. Atmos. Sci.*, **46**, 3144–3176, doi:10.1175/1520-0469(1989)046<3144:EOVWSO>2.0.CO;2.
- , and P. S. Dailey, 1995: The temporal behavior of numerically simulated multicell-type storms. Part I. Modes of behavior. *J. Atmos. Sci.*, **52**, 2073–2095, doi:10.1175/1520-0469(1995)052<2073:TTBONS>2.0.CO;2.
- , and —, 2001: Numerical simulation of the interaction between the sea-breeze front and horizontal convective rolls. Part II: Alongshore ambient flow. *Mon. Wea. Rev.*, **129**, 2057–2072, doi:10.1175/1520-0493(2001)129<2057:NSOTIB>2.0.CO;2.
- , G. L. Mullendore, and S.-H. Kim, 2006: Discrete propagation in numerically simulated nocturnal squall lines. *Mon. Wea. Rev.*, **134**, 3735–3752, doi:10.1175/MWR3268.1.
- Garratt, J. R., 1992: *The Atmospheric Boundary Layer*. Cambridge University Press, 316 pp.
- Gentine, P., A. Garelli, S.-B. Park, J. Nie, G. Torri, and Z. Kuang, 2016: Role of surface heat fluxes underneath cold pools. *Geophys. Res. Lett.*, **43**, 874–883, doi:10.1002/2015GL067262.
- Grady, R. L., and J. Verlinde, 1997: Triple-Doppler analysis of a discretely propagating, long-lived, high plains squall line. *J. Atmos. Sci.*, **54**, 2729–2748, doi:10.1175/1520-0469(1997)054<2729:TDAOAD>2.0.CO;2.
- Grant, L. D., and S. C. van den Heever, 2016: Cold pool dissipation. *J. Geophys. Res. Atmos.*, **121**, 1138–1155, doi:10.1002/2015JD023813.
- Hohenegger, C., P. Brockhaus, C. S. Bretherton, and C. Schär, 2009: The soil moisture–precipitation feedback in simulations with explicit and parameterized convection. *J. Climate*, **22**, 5003–5020, doi:10.1175/2009JCLI2604.1.
- Houze, R. A., 1977: Structure and dynamics of a tropical squall-line system. *Mon. Wea. Rev.*, **105**, 1540–1567, doi:10.1175/1520-0493(1977)105<1540:SADOAT>2.0.CO;2.
- , 2014: *Cloud Dynamics*. 2nd ed. International Geophysics Series, Vol. 104, Academic Press, 496 pp.
- Jakob, C., 2010: Accelerating progress in global atmospheric model development through improved parameterizations: Challenges, opportunities, and strategies. *Bull. Amer. Meteor. Soc.*, **91**, 869–875, doi:10.1175/2009BAMS2898.1.
- , 2014: Going back to basics. *Nat. Climate Change*, **4**, 1042–1045, doi:10.1038/nclimate2445.
- Johnson, R. H., and P. J. Hamilton, 1988: The relationship of surface pressure features to the precipitation and airflow structure of an intense midlatitude squall line. *Mon. Wea. Rev.*, **116**, 1444–1473, doi:10.1175/1520-0493(1988)116<1444:TROSPF>2.0.CO;2.
- Lauwaet, D., N. P. M. van Lipzig, N. Kalthoff, and K. De Ridder, 2010: Impact of vegetation changes on a mesoscale convective system in west Africa. *Meteor. Atmos. Phys.*, **107**, 109–122, doi:10.1007/s00703-010-0079-7.
- Letkewicz, C. E., A. J. French, and M. D. Parker, 2013: Base-state substitution: An idealized modeling technique for approximating environmental variability. *Mon. Wea. Rev.*, **141**, 3062–3086, doi:10.1175/MWR-D-12-00200.1.
- Mahoney, K. M., G. M. Lackmann, and M. D. Parker, 2009: The role of momentum transport in the motion of a quasi-idealized mesoscale convective system. *Mon. Wea. Rev.*, **137**, 3316–3338, doi:10.1175/2009MWR2895.1.
- Marshall, J. H., and D. J. Parker, 2006: Secondary initiation of multiple bands of cumulonimbus over southern Britain. II: Dynamics of secondary initiation. *Quart. J. Roy. Meteor. Soc.*, **132**, 1053–1072, doi:10.1256/qj.05.152.
- Morcrette, C. J., K. A. Browning, A. M. Blyth, K. E. Bozier, P. A. Clark, D. Ladd, E. G. Norton, and E. Pavelin, 2006: Secondary initiation of multiple bands of cumulonimbus over southern Britain. I: An observational case-study. *Quart. J. Roy. Meteor. Soc.*, **132**, 1021–1051, doi:10.1256/qj.05.151.
- NCAR, 2014: NCAR Command Language, version 6.1.2. NCAR, doi:10.5065/D6WD3XH5.
- Oberthaler, A. J., and P. M. Markowski, 2013: A numerical simulation study of the effects of anvil shading on quasi-linear convective systems. *J. Atmos. Sci.*, **70**, 767–793, doi:10.1175/JAS-D-12-0123.1.
- Ogura, Y., and M.-T. Liou, 1980: The structure of a midlatitude squall line: A case study. *J. Atmos. Sci.*, **37**, 553–567, doi:10.1175/1520-0469(1980)037<0553:TSOAMS>2.0.CO;2.
- Parker, M. D., 2008: Response of simulated squall lines to low-level cooling. *J. Atmos. Sci.*, **65**, 1323–1341, doi:10.1175/2007JAS2507.1.
- Pearson, K. J., G. M. S. Lister, C. E. Birch, R. P. Allan, R. J. Hogan, and S. J. Woolnough, 2014: Modelling the diurnal cycle of tropical convection across the ‘grey zone.’ *Quart. J. Roy. Meteor. Soc.*, **140**, 491–499, doi:10.1002/qj.2145.
- Pereira Filho, A. J., M. A. F. Silva Dias, R. I. Albrecht, L. G. P. Pereira, A. W. Gandu, O. Massambani, A. Tokay, and S. Rutledge, 2002: Multisensor analysis of a squall line in the Amazon region. *J. Geophys. Res.*, **107**, 8084, doi:10.1029/2000JD000305.
- Petch, J. C., A. R. Brown, and M. E. B. Gray, 2002: The impact of horizontal resolution on the simulations of convective development over land. *Quart. J. Roy. Meteor. Soc.*, **128**, 2031–2044, doi:10.1256/003590002320603511.
- Redelsperger, J.-L., and Coauthors, 2000: A GCSS model intercomparison for a tropical squall line observed during TOGA-COARE. I: Cloud-resolving models. *Quart. J. Roy. Meteor. Soc.*, **126**, 823–863, doi:10.1002/qj.49712656404.
- , C. D. Thorncroft, A. Diedhiou, T. Lebel, D. J. Parker, and J. Polcher, 2006: African Monsoon Multidisciplinary Analysis: An international research project and field campaign. *Bull. Amer. Meteor. Soc.*, **87**, 1739–1746, doi:10.1175/BAMS-87-12-1739.
- Rotunno, R., J. B. Klemp, and M. L. Weisman, 1988: A theory for strong, long-lived squall lines. *J. Atmos. Sci.*, **45**, 463–485, doi:10.1175/1520-0469(1988)045<0463:ATFSL>2.0.CO;2.
- Roux, F., 1988: The West African squall line observed on 23 June 1981 during COPT 81: Kinematics and thermodynamics of the convective region. *J. Atmos. Sci.*, **45**, 406–426, doi:10.1175/1520-0469(1988)045<0406:TWASLO>2.0.CO;2.
- Schlemmer, L., and C. Hohenegger, 2014: The formation of wider and deeper clouds as a result of cold-pool dynamics. *J. Atmos. Sci.*, **71**, 2842–2858, doi:10.1175/JAS-D-13-0170.1.
- Seifert, A., and D. K. Beheng, 2006: A two-moment cloud microphysics parameterization for mixed-phase clouds. Part 2: Maritime vs. continental deep convective storms. *Meteor. Atmos. Phys.*, **92**, 67–82, doi:10.1007/s00703-005-0113-3.

- Smull, B. F., and R. A. Houze Jr., 1985: A midlatitude squall line with a trailing region of stratiform rain: Radar and satellite observations. *Mon. Wea. Rev.*, **113**, 117–133, doi:[10.1175/1520-0493\(1985\)113<0117:AMSLWA>2.0.CO;2](https://doi.org/10.1175/1520-0493(1985)113<0117:AMSLWA>2.0.CO;2).
- Takemi, T., 2007: Environmental stability control of the intensity of squall lines under low-level shear conditions. *J. Geophys. Res.*, **112**, D24110, doi:[10.1029/2007JD008793](https://doi.org/10.1029/2007JD008793).
- Tawfik, A. B., and P. A. Dirmeyer, 2014: A process-based framework for quantifying the atmospheric preconditioning of surface-triggered convection. *Geophys. Res. Lett.*, **41**, 173–178, doi:[10.1002/2013GL057984](https://doi.org/10.1002/2013GL057984).
- Trier, S. B., W. C. Skamarock, M. A. LeMone, D. B. Parsons, and D. P. Jorgensen, 1996: Structure and evolution of the 22 February 1993 TOGA COARE squall line: Numerical simulations. *J. Atmos. Sci.*, **53**, 2861–2886, doi:[10.1175/1520-0469\(1996\)053<2861:SAEOTF>2.0.CO;2](https://doi.org/10.1175/1520-0469(1996)053<2861:SAEOTF>2.0.CO;2).
- Uijlenhoet, R., M. Steiner, and J. A. Smith, 2003: Variability of raindrop size distributions in a squall line and implications for radar rainfall estimation. *J. Hydrometeor.*, **4**, 43–61, doi:[10.1175/1525-7541\(2003\)004<0043:VORSDI>2.0.CO;2](https://doi.org/10.1175/1525-7541(2003)004<0043:VORSDI>2.0.CO;2).
- Verrelle, A., D. Ricard, and C. Lac, 2015: Sensitivity of high-resolution idealized simulations of thunderstorms to horizontal resolution and turbulence parametrization. *Quart. J. Roy. Meteor. Soc.*, **141**, 433–448, doi:[10.1002/qj.2363](https://doi.org/10.1002/qj.2363).
- Webster, P. J., and R. Lukas, 1992: TOGA COARE: The Coupled Ocean–Atmosphere Response Experiment. *Bull. Amer. Meteor. Soc.*, **73**, 1377–1416, doi:[10.1175/1520-0477\(1992\)073<1377:TTCOR>2.0.CO;2](https://doi.org/10.1175/1520-0477(1992)073<1377:TTCOR>2.0.CO;2).
- Weisman, M. L., and J. B. Klemp, 1982: The dependence of numerically simulated convective storms on vertical wind shear and buoyancy. *Mon. Wea. Rev.*, **110**, 504–520, doi:[10.1175/1520-0493\(1982\)110<0504:TDonSC>2.0.CO;2](https://doi.org/10.1175/1520-0493(1982)110<0504:TDonSC>2.0.CO;2).
- , and R. Rotunno, 2004: “A theory for strong long-lived squall lines” revisited. *J. Atmos. Sci.*, **61**, 361–382, doi:[10.1175/1520-0469\(2004\)061<0361:ATFSL>2.0.CO;2](https://doi.org/10.1175/1520-0469(2004)061<0361:ATFSL>2.0.CO;2).
- , W. C. Skamarock, and J. B. Klemp, 1997: The resolution dependence of explicitly modeled convective systems. *Mon. Wea. Rev.*, **125**, 527–548, doi:[10.1175/1520-0493\(1997\)125<0527:TRDOEM>2.0.CO;2](https://doi.org/10.1175/1520-0493(1997)125<0527:TRDOEM>2.0.CO;2).
- Wolters, D., C. C. van Heerwaarden, J. V.-G. de Arellano, B. Cappelaere, and D. Ramier, 2010: Effects of soil moisture gradients on the path and the intensity of a West African squall line. *Quart. J. Roy. Meteor. Soc.*, **136**, 2162–2175, doi:[10.1002/qj.712](https://doi.org/10.1002/qj.712).
- Zängl, G., D. Reinert, P. Rípodas, and M. Baldauf, 2015: The ICON (ICOsahedral Non-hydrostatic) modelling framework of DWD and MPI-M: Description of the non-hydrostatic dynamical core. *Quart. J. Roy. Meteor. Soc.*, **141**, 563–579, doi:[10.1002/qj.2378](https://doi.org/10.1002/qj.2378).
- Zipser, E. J., 1977: Mesoscale and convective-scale downdrafts as distinct components of squall-line structure. *Mon. Wea. Rev.*, **105**, 1568–1589, doi:[10.1175/1520-0493\(1977\)105<1568:MACDAD>2.0.CO;2](https://doi.org/10.1175/1520-0493(1977)105<1568:MACDAD>2.0.CO;2).